SPECTROSCOPY

Super-resolution lightwave tomography of electronic bands in quantum materials

M. Borsch[1]*, C. P. Schmid[2]*, L. Weigl[2], S. Schlauderer[2], N. Hofmann[2], C. Lange[2]†, J. T. Steiner[3], S. W. Koch[3], R. Huber[2]‡, M. Kira[1]‡

Searching for quantum functionalities requires access to the electronic structure, constituting the foundation of exquisite spin-valley–electronic, topological, and many-body effects. All-optical band-structure reconstruction could directly connect electronic structure with the coveted quantum phenomena if strong lightwaves transported localized electrons within preselected bands. Here, we demonstrate that harmonic sideband (HSB) generation in monolayer tungsten diselenide creates distinct electronic interference combs in momentum space. Locating these momentum combs in spectroscopy enables super-resolution tomography of key band-structure details in situ. We experimentally tuned the optical-driver frequency by a full octave and show that the predicted super-resolution manifests in a critical intensity and frequency dependence of HSBs. Our concept offers a practical, all-optical, fully three-dimensional tomography of electronic structure even in microscopically small quantum materials, band by band.

Band-structure engineering (*1*–*3*) strives to design the dependence of energies and geometric phases (*4*) of electronic states of solids on the wave vector, $\mathbf{k}$. These attributes ultimately control emergent quantum phenomena, ranging from excitons (Coulomb-bound electron-hole pairs) (*5*, *6*) to many-body complexes (*7*) and quantum phase transitions (*8*). Monolayers of transition-metal dichalcogenides, such as tungsten diselenide (WSe_2), host a bounty of such quantum effects (*1*, *6*, *8*, *9*). Angle-resolved photoelectron spectroscopy has championed electronic band-structure mapping (*10*–*13*) in samples of sufficient size, measured at ultrahigh vacuum conditions. All-optical techniques, such as harmonic sideband (HSB) (*14*–*17*) and high-harmonic generation (HHG) (*18*–*27*), promise in situ probing of even microscopically small and/or atomically thin solids in ambient. Yet, HHG mapping encounters challenges: Atomically strong lightwaves inherently spread electrons broadly throughout the Brillouin zone (BZ) (*20*) and induce electronic interferences (*21*) as well as transport among multiple bands.

Such contributions become disentangled in HSB generation, in which an optical field selects electronic bands by resonantly exciting coherences between a specific valence-conduction band pair, creating an electron-hole (*e*-*h*) excitation (Fig. 1A, top red lines). If tuned in resonance with the 1*s* A exciton of monolayer WSe_2, the pulse selectively prepares an excitonic wave packet defined by the microscopic interband polarization $P_{\mathbf{k}}$ (Fig. 1A, color map at time $t = 0$) close to the K point where the energy difference $E^{\mathrm{eh}}_{\mathbf{k}}$ (Fig. 1A, bottom red line) between the two bands is minimal. Unlike in HHG, $P_{\mathbf{k}}$ is strongly localized and oscillates with the frequency ν_{1s} corresponding to the 1*s*-exciton energy, $h\nu_{1s}$ (where h is Planck's constant). A strong multi-terahertz field at a frequency $\nu_{\mathrm{THz}} \ll E^{\mathrm{eh}}_{\mathbf{k}}/h$ then creates HSBs by transporting $P_{\mathbf{k}}$ from the K point to $\mathbf{k}$ (Fig. 1A, color map at $t > 0$). The resulting increase, $E^{\mathrm{eh}}_{\mathbf{k}} - E^{\mathrm{eh}}_{\mathbf{k}=K}$, in the energy of $P_{\mathbf{k}}$ is emitted as HSB radiation, connecting the HSB spectrum with the band structure. Considerable spreading of $P_{\mathbf{k}}$—although much weaker than in HHG—and many-body contributions to the emission energy may complicate a direct inference of $E^{\mathrm{eh}}_{\mathbf{k}}$ from HSB spectra. Nevertheless, the HSB emission can be elegantly linked with $E^{\mathrm{eh}}_{\mathbf{k}}$ because the polarization wave packet $P_{\mathbf{k}}$ starts from the K point and is almost sinusoidally translated by the multiterahertz field (*28*).

The connection of the HSB spectrum with this well-synchronized motion and $E^{\mathrm{eh}}_{\mathbf{k}}$ becomes apparent when $P_{\mathbf{k}}(t) \equiv P^{\mathrm{rot}}_{\mathbf{k}}(t)e^{-2\pi i\nu_{\mathrm{opt}}t}$ is analyzed in a frame rotating with the optical excitation frequency ν_{opt}. The nth HSB is generated if $P^{\mathrm{rot}}_{\mathbf{k}}(t)$ oscillates with the frequency $\nu_n = n\,\nu_{\mathrm{THz}}$, which occurs only if $P^{\mathrm{rot}}_{\mathbf{k}}(t)$ has been translated to a $\mathbf{k}$ value where the HSB-photon energy, $E^{\mathrm{HSB}}_n \equiv h\nu_{\mathrm{opt}} + h\nu_n$, matches the energy of $P_{\mathbf{k}}$—that is, $E^{\mathrm{HSB}}_n = E^{\mathrm{eh}}_{\mathbf{k}}$. As illustrated in Fig. 1B for the 5th HSB, the oscillating polarization, $P^{\mathrm{rot}}_{\mathbf{k}}(t)$ crosses a given $\mathbf{k}$ value twice during a single multiterahertz cycle. In a simplified picture, the multiterahertz field purely translates $P^{\mathrm{rot}}_{\mathbf{k}}(t) = P^{\mathrm{rot}}_{\mathbf{k}(t)}$ with $\mathbf{k}(t) = \mathbf{k} - 2\pi|e|/h\int_{-\infty}^{t}\mathrm{d}t'\,\mathbf{E}_{\mathrm{THz}}(t')$ so that these two crossings (sparks) can be viewed as separate polarization bursts, adding up as a coherent superposition to the total spectral component

$$P^{\mathrm{rot}}_{\mathbf{k}}(\nu_5) = \int \mathrm{d}t\, P^{\mathrm{rot}}_{\mathbf{k}}(t)e^{+2\pi i\nu_5 t} \qquad (1)$$

The phase evolution between these bursts is defined by the spectrum-projecting kernel, $e^{+2\pi i\nu_5 t}$, which oscillates five times faster than

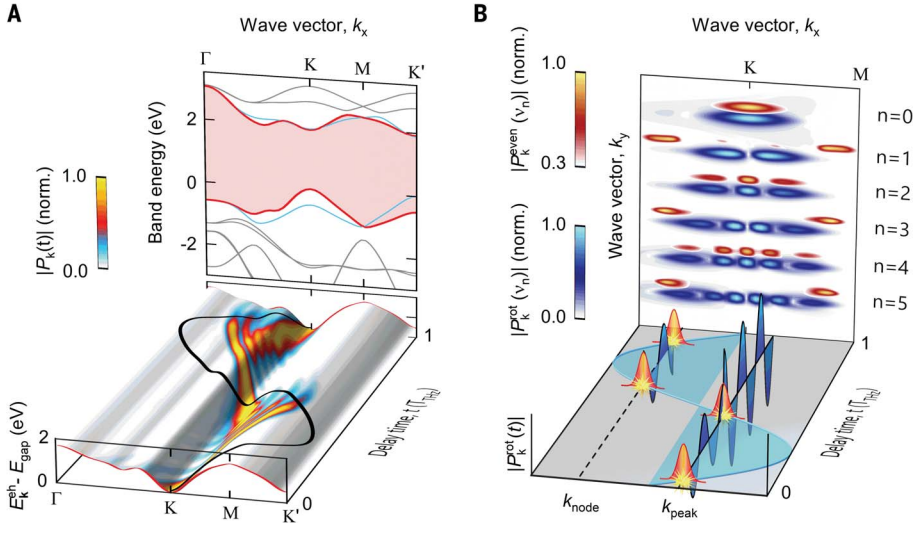

Fig. 1. Harmonic sideband generation and crystal momentum combs. (**A**) Band structure (top) of monolayer WSe_2 and typical exciton wave-packet dynamics (bottom) (color map $|P_k(t)|$ of many-body computation) in HSB. The red lines indicate the *e*-*h* bands, and the thick black line indicates the driving multiterahertz field (cycle duration, $T_{\mathrm{THz}} = \nu^{-1}_{\mathrm{THz}}$), projected onto the $E^{\mathrm{eh}}_{\mathbf{k}}$ surface (gray). (**B**) Schematics of a $|P^{\mathrm{rot}}_{\mathbf{k}}(t)|$ (Gaussians) on a sinusoidal path (transparent area) crossing a given $\mathbf{k}$ point twice during a multiterahertz cycle. These crossings (sparks) yield HSB-emission contributions interfering as waves (blue shaded areas). The screen compares $\mathbf{k}$ combs (blue-white color maps) with their even parts (red-yellow color maps) for 0th to 5th HSBs on the basis of full many-body computations.

[1]Department of Electrical Engineering and Computer Science, University of Michigan, Ann Arbor, MI, USA. [2]Department of Physics, University of Regensburg, Regensburg, Germany. [3]Department of Physics, University of Marburg, Marburg, Germany.
*These authors contributed equally to this work.
†Present address: Fakultät Physik, Technische Universität Dortmund, Otto-Hahn-Straße 4, 44227 Dortmund, Germany.
‡Corresponding author. Email: mackkira@umich.edu (M.K.); rupert.huber@ur.de (R.H.)

the $\mathbf{k}(t)$ trajectory (Fig. 1B, light blue area). Hence, there are, respectively, six or five $\mathbf{k}$ values where the first and second bursts are in (Fig. 1B, solid line) or out of phase (Fig. 1B, dashed line), leading to interference maxima or minima. Generally, $P_{\mathbf{k}}^{\mathrm{rot}}(\nu_n)$ exhibits a $\mathbf{k}$-space interference pattern with $(n + 1)$ maxima (screen), which we call a $\mathbf{k}$ comb in analogy to frequency combs (*29*, *30*) created by multiple time-domain pulses. Because $\mathbf{k}$ combs are the projections of $P_{\mathbf{k}}^{\mathrm{rot}}(t)$ (having the energy $E_{\mathbf{k}}^{\mathrm{eh}}$) onto a given $h\nu_n$, their amplitude decreases with increasing HSB-to-band energy difference.

In reality, $P_{\mathbf{k}}^{\mathrm{rot}}(t)$ cannot be reduced to a simple $\mathbf{k}(t)$ translation because many-body interactions distort the path, dephase the polarization, and renormalize the emission energies. We performed full quantum-kinetic computations with a state-of-the-art dynamic cluster-expansion approach (supplementary materials) (*5*) to systematically predict the HSB properties on the basis of fundamental electronic band structure, geometric phase effects, and the strong light-matter as well as the many-body Coulomb interactions. Although many-body and interference effects spread $P_{\mathbf{k}}$ and create new oscillating features (Fig. 1A, blue regions), the $(n + 1)$–peak structure of $\mathbf{k}$ combs remains robust (Fig. 1B, blue color maps). At the K point, all $\mathbf{k}$ combs of odd order exhibit a node, whereas those of even order feature a peak, implying a dominantly odd and even symmetry, respectively. This symmetry can be broken only by transporting $P_{\mathbf{k}}^{\mathrm{rot}}(t)$ to inversion asymmetric regions of the bands where $E_{\mathbf{k}}^{\mathrm{eh}} \neq E_{-\mathbf{k}}^{\mathrm{eh}}$.

Because $P_{\mathbf{k}}$ defines the coherent transition amplitude for *e*-*h* recombination (*5*) associated with the dipole moment $d_{\mathbf{k}}$, its symmetry affects the total HSB intensity

$$I_{\mathrm{HSB}}(\nu) \propto \left| (\nu_{\mathrm{opt}} + \nu) \sum_{\mathbf{k}\in \mathrm{BZ}} d_{\mathbf{k}} P_{\mathbf{k}}^{\mathrm{rot}}(\nu) \right|^2 \quad (2)$$

where the $\mathbf{k}$ sum includes the entire BZ. For symmetric systems ($E_{\mathbf{k}}^{\mathrm{eh}} = E_{-\mathbf{k}}^{\mathrm{eh}}$ and $d_{\mathbf{k}} = d_{-\mathbf{k}}$), odd-order sidebands vanish because the odd-order $\mathbf{k}$ combs eliminate the total sum in $I_{\mathrm{HSB}}(\nu)$. Monolayer WSe_2 has inversion symmetric bands close to the K point, with asymmetric features ($E_{\mathbf{k}}^{\mathrm{eh}} \neq E_{-\mathbf{k}}^{\mathrm{eh}}$) emerging toward the M point. Only the even part of each comb, $P_{\mathbf{k}}^{\mathrm{even}}(\nu_n) \equiv \frac{1}{2}[P_{\mathbf{k}}^{\mathrm{rot}}(\nu_n) + P_{-\mathbf{k}}^{\mathrm{rot}}(\nu_n)]$, contributes to $I_{\mathrm{HSB}}(\nu_n)$, assuming that $d_{\mathbf{k}}$ is symmetric. $P_{\mathbf{k}}^{\mathrm{even}}(\nu_n)$ (Fig. 1B, red color map) for n = 0, 2, and 4 closely follows the respective $\mathbf{k}$ comb (Fig. 1B, blue color map). In stark contrast, odd orders produce a $P_{\mathbf{k}}^{\mathrm{even}}(\nu_n)$ that vanishes over the inversion-symmetric region of the bands and peaks sharply at the onset of the band asymmetry. Thus, odd-order sidebands solely originate from the outermost comb line. Although the $P_{\mathbf{k}}^{\mathrm{even}}(\nu_n)$ of the even HSBs are not localized, their $\mathbf{k}$ combs have a sharp leading edge whose energy and momentum overlap with the band structure determines the strength of the respective HSB emission. In any case, the position of the outermost comb line locates the origin of HSB at

$$k(n) = \frac{|e|E_{\mathrm{THz}}}{h\nu_{\mathrm{THz}}} C_n(E_{\mathrm{THz}}, \nu_{\mathrm{THz}}) \quad (3)$$

which can be interpreted as the maximum excursion of a classical trajectory times a many-body quantum correction C_n. The latter typically assumes a value between 0.5 and 1.5. The super-resolution follows as the width of the outermost comb line locates the nth HSB emission to an $(n + 1)$ times narrower $\mathbf{k}$ range than the excursion scale of the wave packets (supplementary materials), which improves the $\mathbf{k}$ resolution linearly with n. The vectorial position of the $\mathbf{k}$ comb is assigned by $k(n)$ times the direction of the multiterahertz field.

To show that super-resolution prominently manifests in experimental HSB spectra, we resonantly excited the 1*s* A exciton resonance in monolayer WSe_2 with an optical pulse (duration, 100 fs) centered at the photon energy of $h\nu_{\mathrm{opt}}$ = 1.665 eV. A linearly polarized multiterahertz transient centered at ν_{THz} = 42 THz accelerates $P_{\mathbf{k}}$ (supplementary materials) along the Γ-K direction. We controlled $k(n)$ by tuning the peak electric field $E_{\mathrm{THz}}^{\mathrm{peak}}$ from 7 to 19 MV cm^{-1} (in vacuum). The shape of the HSB spectra (Fig. 2A) changes strongly as function of $E_{\mathrm{THz}}^{\mathrm{peak}}$ and covers the entire visible spectrum. The third-order sideband emerges only for the highest fields, whereas the 5th order sets in steeply at $E_{\mathrm{THz}}^{\mathrm{peak}} = 7$ MV cm^{-1}, reaches its maximum at 13 MV cm^{-1}, and decreases for yet stronger fields (Fig. 2C). The 4th order exhibits a nonmonotonic scaling, too (supplementary materials), albeit not as steep as that of the 5th.

To connect this characteristic scaling behavior with the $\mathbf{k}$ combs, we compared the experiment with our full many-body computations. All HSB spectra (Fig. 2B) and the intensity scaling agree quantitatively, as shown for the 5th-order sideband in Fig. 2C. This allows us to faithfully assign a specific crystal momentum $k(5)$ (Fig. 2C, bottom scale) to each $E_{\mathrm{THz}}^{\mathrm{peak}}$ value (Fig. 2C, top scale) using Eq. 3. The computed $|P_{\mathbf{k}}^{\mathrm{even}}(\nu_5)|^2$ combs (Fig. 2D, color map) and $k(5)$ (Fig. 2D, blue lines) are shown in Fig. 2D as a function of $E_{\mathrm{THz}}^{\mathrm{peak}}$. In Fig. 2E, the corresponding dispersion relation $E_{\mathbf{k}}^{\mathrm{eh}}$ (dark area) is superimposed with $E_{-\mathbf{k}}^{\mathrm{eh}}$ (dotted line) to easily identify the band asymmetry ($E_{\mathbf{k}}^{\mathrm{eh}} \neq E_{-\mathbf{k}}^{\mathrm{eh}}$). The onset of the 5th HSB intensity (Fig. 2C) occurs precisely when $k(5)$ passes the band asymmetry (Fig. 2, C to E, arrow), verifying the super-resolution connection of odd-order HSB intensity and the position of the outermost comb line. Shifting the $\mathbf{k}$ comb further by larger $E_{\mathrm{THz}}^{\mathrm{peak}}$ inevitably increases the central energy of the polarization compared with that of the 5th HSB (Fig. 2E, blue line), reducing the energetic overlap, and thus decreases the 5th HSB intensity. Such a sharp $E_{\mathrm{THz}}^{\mathrm{peak}}$-dependent maximum in HSB intensity signifies a distinctive super-resolution signature for HSB spectroscopy. We verified similar but slightly less stringent super-resolution for even HSBs (supplementary materials).

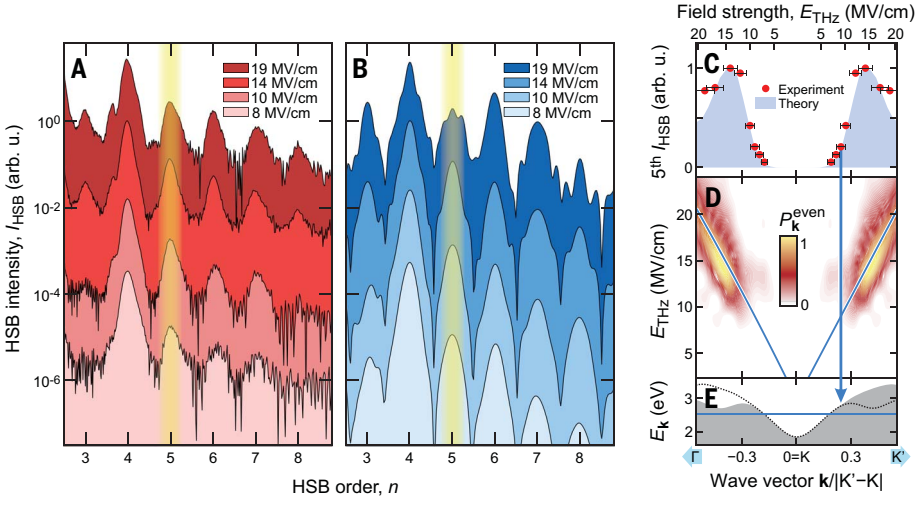

Fig. 2. Super-resolution band-structure tomography with a field-strength scan. (**A**) Measured versus (**B**) computed HSB intensity spectra for different E_{THz} (shifted for visibility) at fixed ν_{THz} = 42 THz. The 5th HSB intensity, I_{HSB}, includes the spectral range of the yellow transparent regions. (**C**) E_{THz} dependence (top axis) of measured (circles and error bars) and computed (shaded area) 5th I_{HSB}. The corresponding $k(5)$ is assigned in the bottom axis by using Eq. 3. (**D**) The computed E_{THz} dependence of the symmetric part of $|P_{\mathbf{k}}^{\mathrm{even}}(\nu_5)|$ and the comb position (blue line). (**E**) Electron-hole dispersion (gray area) in units of the K-to-K′ valley separation $|K' - K|$ and $E_{-\mathbf{k}}^{\mathrm{eh}}$ (dotted line) are connected with the HSB and $\mathbf{k}$ comb through the blue arrow.

To tomographically scan the $k(n)$–dependent crossing of the $\mathbf{k}$ comb with $E^{\mathrm{eh}}_{\mathbf{k}}$, we have developed a setup to quantitatively compare HSB spectra while varying ν_{THz} over a full optical octave, from 27 to 54 THz. The field strength is fixed at $E^{\mathrm{peak}}_{\mathrm{THz}} = 14$ MV cm^{-1} to ensure efficient sideband generation (Fig. 3A) while suppressing parasitic interband excitations by the multiterahertz field. The 5th HSB is essentially absent for $\nu_{\mathrm{THz}} = 27$ THz, sets on sharply for larger THz frequencies (Fig. 3C), and peaks at around 40 THz. The computed spectra (Fig. 3B) and their scaling behavior as function of ν_{THz} (Fig. 3B) reproduce all these signatures very well. The ν_{THz} dependence of $|P^{\mathrm{even}}_{\mathbf{k}}(\nu_5)|^2$ (Fig. 3D, color map) confirms that the HSB peak coincides with the $\mathbf{k}$-comb peak (Fig. 3D, blue arrow) for $\nu_{\mathrm{THz}} = 42$ THz, where the single comb line (Fig. 3D, blue line) both overlaps with the asymmetric region ($E^{\mathrm{eh}}_{\mathbf{k}} \neq E^{\mathrm{eh}}_{-\mathbf{k}}$) (Fig. 3D, solid versus dashed lines) and has an energy close to the polarization ($E^{\mathrm{eh}}_{\mathbf{k}}$). For other ν_{THz} values, the HSB intensity becomes weaker because the $\mathbf{k}$ comb either does not reach the asymmetric range (high ν_{THz}) or differs substantially from the band energy (low ν_{THz}), creating a narrow ν_{THz}-dependent peak in the 5th HSB.

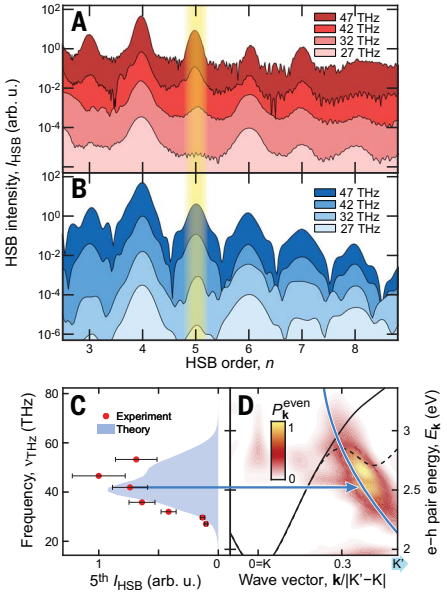

Fig. 3. Super-resolution band-structure tomography with a frequency scan. (**A**) Measured versus (**B**) computed HSB intensity spectra for different multiterahertz frequencies ν_{THz} (shifted for visibility), at fixed $E_{\mathrm{THz}} = 14$ MV/cm. The yellow regions indicate the spectral range of the 5th I_{HSB}. (**C**) Measured (circles and error bars) and computed (shaded) 5th-order I_{HSB} as function of ν_{THz} (scale left) and the corresponding HSB energy (scale right). (**D**) The 5th HSB $\mathbf{k}$-comb position (blue line), $k(5)$ from Eq. 3 in units of the K-to-K′ valley separation $|K' - K|$, and symmetric part of $|P^{\mathrm{even}}_{\mathbf{k}}(\nu_5)|^2$ (color map) as function of ν_{THz} (left) and band energy (right) are compared with the electron-hole energy (solid line) and $E^{\mathrm{eh}}_{-\mathbf{k}}$ (dashed line). The blue arrow assigns the peak HSB-emission conditions.

These combined experimental and theoretical results herald super-resolution lightwave tomography: Because the $\mathbf{k}$ combs localize the HSB emission to a single ($\mathbf{k}$, energy)–point whose connection to the experimental parameters (E_{THz}, ν_{THz}) is known, scanning (E_{THz}, ν_{THz}) tomographically maps $E^{\mathrm{eh}}_{\mathbf{k}}$. Shown in Fig. 4 is the computed HSB intensity, $I_{\mathrm{HSB}}(\nu_n)$, resulting from a comprehensive (E_{THz}, ν_{THz}) scan, each point assigned to a single $[k(n), E^{\mathrm{HSB}}_n]$ pair by means of Eq. 3, for $n = 3, 4, 5, 6$ (Fig. 4, A to D) together with the $E^{\mathrm{eh}}_{\mathbf{k}}$ (solid lines) and $E^{\mathrm{eh}}_{-\mathbf{k}}$ (dashed lines) bands. The edges of $I_{\mathrm{HSB}}(\nu_n)$ track the entire band structure in remarkable detail, confirming that the overlap of the $\mathbf{k}$ combs with the band structure defines the strength of the HSB emission. As a stress test for our tomography, we measured the same $I_{\mathrm{HSB}}(\nu_n)$ with one-dimensional E_{THz} and ν_{THz} scans across few band-structure features and calibrated the experiment-theory intensities with a single factor that does not affect the assessed (E_{THz}, ν_{THz}) dependence. The experimental HSB scans (Fig. 4, A to D, within black bars) and the computations match nearly perfectly.

Also, the microscopic dipole, $d_{\mathbf{k}}$, affects the HSB intensity Eq. 3, which may distort the tomography by overemphasizing momentum regimes with large $d_{\mathbf{k}}$. However, super-resolution of a $\mathbf{k}$ comb locates the odd-order HSBs to a single pair ($\mathbf{k}$, energy), whereas $d_{\mathbf{k}}$ changes slowly over the $\mathbf{k}$ comb. Consequently, taking ratios of two HSB intensities, such as $R_{5\mathrm{th}/3\mathrm{rd}} \equiv I_{\mathrm{HSB}}(\nu_5)/I_{\mathrm{HSB}}(\nu_3)$, eliminates distortions by $d_{\mathbf{k}}$. In Fig. 4E, blue color maps show the first positive peak of gradient $\frac{\partial}{\partial k} R_{5\mathrm{th}/3\mathrm{rd}}$, and red color maps show the first negative peak of gradient $\frac{\partial}{\partial \mathrm{energy}} R_{5\mathrm{th}/3\mathrm{rd}}$, starting from the K point (2 eV) to locate $E^{\mathrm{eh}}_{\mathbf{k}}$ (Fig. 4E, solid line). The resulting $R_{5\mathrm{th}/3\mathrm{rd}}$ gradients track the band dispersion close to the band asymmetry, as expected for the odd $\mathbf{k}$ combs (HSBs), more accurately than the raw HSB intensities (Fig. 4, A and C). Nevertheless, $d_{\mathbf{k}}$ can be measured most sensitively through the rich details of HSB spectra (supplementary materials). The same analysis is repeated for the ratio of 6th and 4th HSBs in Fig. 4F for $\frac{\partial}{\partial \mathbf{k}} R_{6\mathrm{th}/4\mathrm{th}}$ (blue color maps), $\frac{\partial}{\partial \mathrm{energy}} R_{6\mathrm{th}/4\mathrm{th}}$ (red color maps), and $E^{\mathrm{eh}}_{\mathbf{k}}$ (black line). The peaks of these gradients track the band dispersion, although less sharply than for the odd HSBs because the latter benefits from super-resolution, as discussed above. The gradient approach also allows us to unfold the left- and right-hand side of the bands with respect to the K point. We have furthermore verified that using $C_n = 1.3$ in Eq. 3 yields only minor tomographic aberrations, making purely experimental super-resolution tomography possible, whereas fixing these aberrations yields a nontrivial value of C_n and thus experimental access to intriguing many-body effects in quantum materials (supplementary materials).

We introduce a powerful all-optical band-structure tomography by merging three complementary advantages of the harmonic sideband generation: An optical field selects a pair of

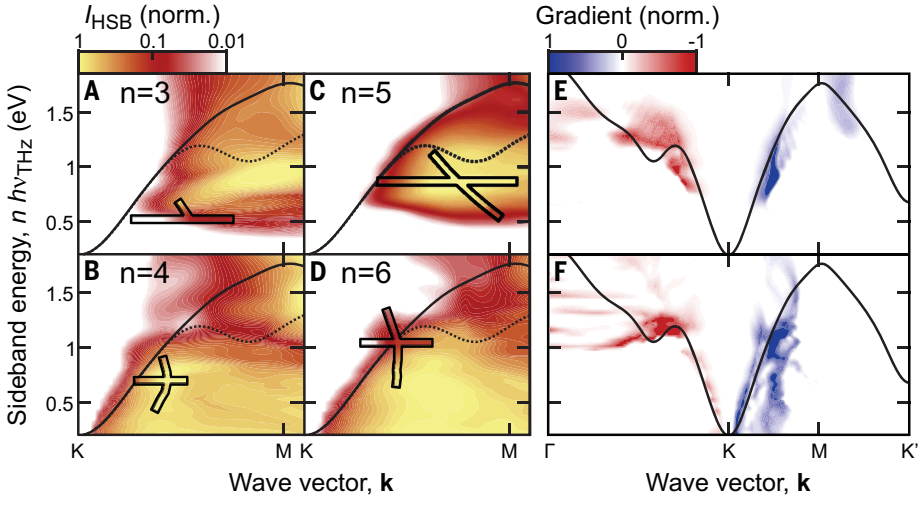

Fig. 4. Super-resolution lightwave tomography. (**A** to **D**) Color maps show the computed (A) 3rd, (B) 4th, (C) 5th, and (D) 6th HSB intensity constructed from a comprehensive (E_{THz}, ν_{THz}) scan and compared with one-dimensional experimental (E_{THz} and ν_{THz}) scans (black boxes). Each (E_{THz}, ν_{THz}) is connected with the wave vector by using Eq. 3 and the nth HSB energy $h(\nu_{\mathrm{opt}} + n\nu_{\mathrm{THz}})$. Also, the electron-hole dispersion (black line) and $E^{\mathrm{eh}}_{-\mathbf{k}}$ (dotted line) are shown. (**E** and **F**) Computed gradients of 5th:3rd (E) and 6th:4th (F) HSB taken in $\mathbf{k}$ (blue color map) and energy (red color map) directions, compared with the $E^{\mathrm{eh}}_{\mathbf{k}}$ (black line); only the first encountered gradient peaks are shown.

valence and conduction bands at a time, a strong multiterahertz field introduces crystal-momentum combs (**k** combs) that localize the origin of the emission to a small region within these bands, and the resulting excitations directly involve the quasiparticles relevant for quantum effects. The **k** combs are demonstrated to deliver a super-resolution lightwave tomography of quantum materials by using one- and two-dimensional multiterahertz frequency–field strength scans. Our approach can be straightforwardly generalized for a fully three-dimensional band tomography by adding the direction of the multiterahertz field as the third scanned variable. Also, geometric phase effects can be characterized by measuring the polarization of the sideband emission with respect to optical excitation. The introduced methodology seems optimally suited for high-precision characterization and control of quantum materials such as two-dimensional monolayer heterostructures, even on microscopic scales.

REFERENCES AND NOTES

1. A. K. Geim, I. V. Grigorieva, *Nature* **499**, 419–425 (2013).
2. M. Schwarze *et al*., *Science* **352**, 1446–1449 (2016).
3. M. S. Rudner, N. H. Lindner, *Nat. Rev. Phys.* **2**, 229–244 (2020).
4. E. Cohen *et al*., *Nat. Rev. Phys.* **1**, 437–449 (2019).
5. M. Kira, S. W. Koch, *Semiconductor Quantum Optics* (Cambridge Univ. Press, 2011).
6. H. Yu, X. Cui, X. Xu, W. Yao, *Natl. Sci. Rev.* **2**, 57–70 (2015).
7. A. E. Almand-Hunter *et al*., *Nature* **506**, 471–475 (2014).
8. Y. Cao *et al*., *Nature* **556**, 43–50 (2018).
9. K. F. Mak, C. Lee, J. Hone, J. Shan, T. F. Heinz, *Phys. Rev. Lett.* **105**, 136805 (2010).
10. T. Ohta, A. Bostwick, T. Seyller, K. Horn, E. Rotenberg, *Science* **313**, 951–954 (2006).
11. Y. L. Chen *et al*., *Science* **325**, 178–181 (2009).
12. J. Reimann *et al*., *Nature* **562**, 396–400 (2018).
13. B. Lv, T. Qian, H. Ding, *Nat. Rev. Phys.* **1**, 609–626 (2019).
14. B. Zaks, R. B. Liu, M. S. Sherwin, *Nature* **483**, 580–583 (2012).
15. F. Langer *et al*., *Nature* **533**, 225–229 (2016).
16. H. B. Banks *et al*., *Phys. Rev. X* **7**, 041042 (2017).
17. F. Langer *et al*., *Nature* **557**, 76–80 (2018).
18. A. H. Chin, O. G. Calderón, J. Kono, *Phys. Rev. Lett.* **86**, 3292–3295 (2001).
19. S. Ghimire *et al*., *Nat. Phys.* **7**, 138–141 (2011).
20. O. Schubert *et al*., *Nat. Photonics* **8**, 119–123 (2014).
21. M. Hohenleutner *et al*., *Nature* **523**, 572–575 (2015).
22. G. Vampa *et al*., *Phys. Rev. Lett.* **115**, 193603 (2015).
23. M. Sivis *et al*., *Science* **357**, 303–306 (2017).
24. N. Tancogne-Dejean, O. D. Mücke, F. X. Kärtner, A. Rubio, *Phys. Rev. Lett.* **118**, 087403 (2017).
25. T. Higuchi, C. Heide, K. Ullmann, H. B. Weber, P. Hommelhoff, *Nature* **550**, 224–228 (2017).
26. N. Yoshikawa, T. Tamaya, K. Tanaka, *Science* **356**, 736–738 (2017).
27. A. J. Uzan *et al*., *Nat. Photonics* **14**, 183–187 (2020).
28. F. Bloch, *Z. Phys.* **52**, 555–600 (1929).
29. J. L. Hall, *Rev. Mod. Phys.* **78**, 1279–1295 (2006).
30. N. Picqué, T. W. Hänsch, *Nat. Photonics* **13**, 146–157 (2019).
31. M. Borsch, Data for figures: Super-resolution lightwave tomography of electronic bands in quantum materials. Zenodo (2020).

ACKNOWLEDGMENTS

We thank F. Langer for technical support and scientific discussions. **Funding:** The Michigan portion of this collaboration is supported by the Army Research Office (ARO) through award W911NF1810299 and College of Engineering Blue Sky Research Program, the Regensburg effort by the Deutsche Forschungsgemeinschaft (DFG; German Research Foundation)–Project-ID, 314695032–SFB 1277 (Subproject A05) and project HU1598/8, and the Marburg part by DFG, Project-ID 223848855-SFB 1083. **Author contributions:** M.B., C.P.S., L.W., S.S., N.H., C.L., J.T.S., S.W.K., R.H., and M.K. conceived the study. M.B., J.T.S., S.W.K., and M.K. developed and performed the many-body computations and analyzed the data. C.P.S., L.W., S.S., N.H., C.L., and R.H. carried out the experiment and analyzed the data. All authors discussed the results and contributed to the writing of the manuscript. **Competing interests:** None declared. **Data and materials availability:** All data presented in the figures are accessible online (*31*). All other data needed to evaluate the conclusions in the paper are present in the paper or the supplementary materials.

SUPPLEMENTARY MATERIALS

science.sciencemag.org/content/370/6521/1204/suppl/DC1
Materials and Methods
Supplementary Text
Figs. S1 to S7
References (*32*–*43*)

7 August 2020; accepted 28 October 2020
10.1126/science.abe2112

Super-resolution lightwave tomography of electronic bands in quantum materials

M. Borsch, C. P. Schmid, L. Weigl, S. Schlauderer, N. Hofmann, C. Lange, J. T. Steiner, S. W. Koch, R. Huber and M. Kira

Science **370** (6521), 1204-1207.
DOI: 10.1126/science.abe2112

Probing quantum materials

Unraveling the functionalities of quantum materials such as spin-valley-electronic, topological, and many-body effects provides a route to exploiting these materials for applications. Borsch *et al.* introduce a spectroscopic technique based on the concept of crystal-momentum combs. By extending the ideas of frequency combs of metrology and superresolution imaging, they demonstrate the ability to directly map out the properties of quantum electronic structures under ambient conditions. Using this technique combined with accurate many-body computations, they were able to reveal tomographic images of two-dimensional quantum materials.

Science, this issue p. 1204